J. Fluid Mech. (2009), vol. 625, pp. 47–74. © 2009 Cambridge University Press
doi:10.1017/S0022112008005491 Printed in the United Kingdom

Saltating particles in a turbulent boundary layer: experiment and theory

M. CREYSSELS[1], P. DUPONT[2], A. OULD EL MOCTAR[3],
A. VALANCE[1]† I. CANTAT[1,4], J. T. JENKINS[1,4], J. M. PASINI[4]‡
AND K. R. RASMUSSEN[5]

[1]IPR, Université de Rennes 1, CNRS UMR 6251, Campus Beaulieu, 35042 Rennes, France
[2]LGCGM, INSA de Rennes, Campus Beaulieu, 35043 Rennes, France
[3]Thermocinétique, Polytech. Nantes, CNRS UMR 6607, 44306 Nantes, France
[4]Department of Theoretical and Applied Mechanics, Cornell University, Ithaca, NY 14853, USA
[5]Department of Earth Sciences, University of Aarhus, DK-8000 Aarhus C, Denmark

(Received 17 July 2008 and in revised form 2 December 2008)

The work presented here focuses on the analysis of a turbulent boundary layer saturated with saltating particles. Experiments were carried out in a wind tunnel 15 m long and 0.6 m wide at the University of Aarhus in Denmark with sand grains 242 μm in size for wind speeds ranging from the threshold speed to twice its value. The saltating particles were analysed using particle image velocimetry (PIV) and particle-tracking velocimetry (PTV), and vertical profiles of particle concentration and velocity were extracted. The particle concentration was found to decrease exponentially with the height above the bed, and the characteristic decay height was independent of the wind speed. In contrast with the logarithmic profile of the wind speed, the grain velocity was found to vary linearly with the height. In addition, the measurements indicated that the grain velocity profile depended only slightly on the wind speed. These results are shown to be closely related to the features of the splash function that characterizes the impact of the saltating particles on a sandbed. A numerical simulation is developed that explicitly incorporates low-velocity moments of the splash function in a calculation of the boundary conditions that apply at the bed. The overall features of the experimental measurements are reproduced by simulation.

1. Introduction

When a wind blowing over an initially immobile bed of cohesionless grains becomes sufficiently strong, grains in the size range of 100–500 μm begin to jump over the surface. This saltation is the primary mode of the initial sand movement (Bagnold 1941). Stronger winds can involve a sufficient number of grains so that collisions above the bed become important (Sørensen & McEwan 1996; Jenkins & Hanes 1998), and direct suspension by the turbulent velocity fluctuations may take place (Pasini & Jenkins 2005).

To initiate saltation, a grain may be lifted from the bed by a strong, localized turbulent eddy. Then, the drag of the air on the grain accelerates it, and it collides

---

† Email address for correspondence: alexandre.valance@univ-rennes1.fr
‡ Present address: United Technologies Research Center, 411 Silver Lane, East Hartford, CT 06108,USA

with the bed with increased momentum. Impacting grains rebound and eject other grains that may also be accelerated by the wind until a sufficient number of grains are participating in the process to diminish the wind near the bed and create a steady balance in the exchanges of momentum between the grains and the wind and the grains and the bed.

Experimental, numerical and analytical studies have been carried out in attempts to understand and predict the process of saltation. For example, the total grain flux and the wind profile within the saltation layer have been measured in wind tunnels and the field (Rasmussen & Mikkelsen 1991, 1998; White & Mounla 1991; McKenna-Neuman & Maljaars 1997; Iversen & Rasmussen 1999; Namikas 2003; Liu & Dong 2004). Numerical simulations have also been undertaken (Ungar & Haff 1987; Anderson & Haff 1988, 1991; Werner 1990) and analytical models proposed (Owen 1964; Sørensen 1991, 2004; Sauermann, Kroy & Herrmann 2001; Andreotti 2004; Duran & Herrmann 2006) to explain the empirical findings. The numerical simulations and analytical models all have the capacity to predict the observed variation of the total grain flux with the strength of the wind and the observed features of the velocity profile of the wind. However, to determine inputs to the simulations and check the assumptions made in the models, it is necessary to have direct measurements of the particle behaviour near the bed.

Particle trajectories have been studied using high-speed photography (White & Schulz 1977; Napalnis, Hunt & Barrett 1993; Nishimura & Hunt 2000) that permits the variation of the grain speed with the height to be obtained but, unfortunately, only for very small particle concentrations. In recent years, laser-based methods, such as laser Doppler anemometry (LDA; Liu & Dong 2004; Rasmussen & Sørensen 2005), and particle-imaging techniques, such as particle image velocimetry (PIV; Yang *et al.* 2007) and particle-tracking velocimetry (PTV), have become available for directly measuring the particle speed in the saltation layer.

The behaviour of the particles near the bed includes information on the splash process, in which a grain impacts the bed, rebounds and ejects other grains. However, because of the large concentration and velocity gradients very near the bed, it is difficult to make reliable measurements there in wind tunnels or in the field. As a consequence, the splash process has been analysed under somewhat artificial conditions: in computer simulations (Werner & Haff 1988; Anderson & Haff 1991; Oger *et al.* 2005), in wind tunnel experiments with very small transport rates (Willetts & Rice 1989; Rice, Willetts & McEwan 1996) and by propelling a single particle (Mitha *et al.* 1986; Rioual, Valance & Bideau 2000; Beladjine *et al.* 2007) or a sand grain (Werner 1990) into a static bed of similar particles.

In previous numerical simulations to determine a steady distribution of particle velocities (Werner 1990; Anderson & Haff 1991), collisions between particles above the bed are neglected, and the particles are assumed to be influenced only by gravity and the drag of the wind. Trajectories of particles with a range of initial velocities at the bed are followed until the particles return to the bed. Simultaneously, the evolution of the distribution of particle velocities with height is calculated; this permits the determination of the profiles of particle concentration and particle shear stress, calculated as averages, from it. The local value of the particle shear stress is then used to update the wind profile using a mixing-length assumption based on the local fluid shear stress.

At the bed, the velocity distribution of the incoming particles is related to that of the outgoing particles through a ‘splash function’ (Ungar & Haff 1987). Werner (1990), for example, determined a splash function from experiments on impacts of grains on a bed. Using it in his simulation, he found that the wind profiles obtained over a range of wind speeds exhibited a sharp focus point, conjectured to exist by Bagnold (1941), above which the velocity increased with increasing wind speed and below which the velocity decreased with increasing wind speed. Associated with this is a decrease in the fluid shear stress at the bed with increasing wind speed.

This is in conflict with the assumption made by Owen (1964) and adopted by Sauermann *et al.* (2001) and Sørensen (2004) that once steady saltation is reached, the fluid shear stress at the bed is always equal to its value at the threshold for saltation. On the other hand, Sørensen (2004) shows that this assumption does yield an expression for the total mass flux which, when scaled by the cube of the friction velocity and plotted against it, exhibits a maximum, in accord with experiment (Iversen & Rasmussen 1999). Duran & Herrmann (2006) show how the maximum in the flux is obtained from Sorensen's (2004) arguments when Owen's (1964) assumption is relaxed.

Numerical simulations that determine the form of the steady velocity distribution function are clearly useful in testing theories. However, they are computationally expensive, and the complexity of both their inputs and the calculations made upon them makes it difficult to determine the mechanisms that lead to their results. What is required to make further progress on understanding saltation are more and better data on the particle properties above the bed and simpler numerical simulations.

In this paper, the results of combined measurements of the velocity and concentration of saltating particles in a turbulent boundary layer using PTV, PIV and LDA imaging techniques are presented. Then, the average and the first velocity moment of the splash function (Beladjine *et al.* 2007) are employed to calculate the average exchange of particles and particle momentum at the surface of the bed in steady conditions. For this, the velocity distribution of the ejected particles is assumed to be half-Gaussian. Two of the three parameters that characterize the distribution function are determined by the balance of mass and vertical momentum between the flow and the bed. The remaining parameter is solved for in a simple and rapid numerical simulation of particles with a half-Gaussian distribution of initial vertical velocities interacting with and influencing the turbulent shearing flow before returning to the bed.

The simple numerical simulation is found to reproduce most of the measured features of the flow of both the gas and the particles. These include the shape of the profiles of the average gas and grain velocities, the exponential decay of the concentration and the measured dependence of the total particle flux on the Shields parameter. The significant difference between the results of the numerical simulation and the measurements is the prediction of the magnitude of the grain velocity.

In any case, the fact that a numerical simulation that employs a single free parameter reproduces the observed features of steady saltation opens the possibility of developing a better understanding of the process. What remains to do is to determine an expression for the particle shear stress above the bed in terms of the concentration, the average particle and gas velocities and, perhaps, measures of their variability (Pasini & Jenkins 2005). This may be determined from an appropriate characterization of data or might be obtained from the simulation itself.

2. Instruments and methods

Note that for the sake of clarity, dimensional forms of quantities are indicated by a hat, to distinguish them from their dimensionless counterparts.

S^*	$\hat{u}^*$ (m s^{-1})	$\hat{y}_0$ (mm)	$\hat{Q}$ (g m^{-1} s^{-1})
0.012	0.24	0.04	5.25
0.022	0.32	0.13	12.84
0.035	0.40	0.28	21.09
0.050	0.48	0.46	32.00
0.068	0.56	0.66	48.85
0.098	0.67	0.93	79.55

TABLE 1. Features of the different experimental runs. The Shields parameter S^* is $\hat{\rho}_f\hat{u}^{*2}/(\hat{\rho}_p\hat{g}\hat{d})$, where $\hat{\rho}_f$ is the mass density of the fluid; $\hat{\rho}_p$ is the mass density of the material of the particles; $\hat{g}$ is the gravitational acceleration; and $\hat{d}$ the particle diameter. The relative uncertainty on the measurements of $\hat{u}^*$, $\hat{y}_0$ and $\hat{Q}$ is respectively 5 %, 50 % and 5 %.

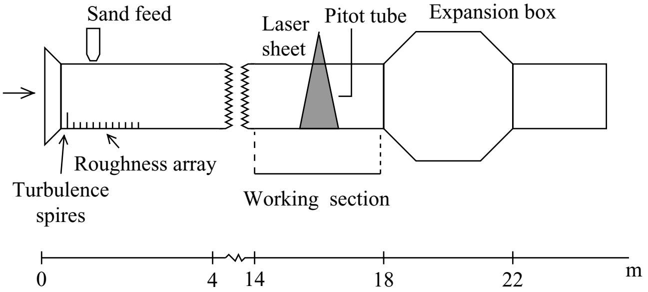

FIGURE 1. Sketch of the wind tunnel.

2.1. *Experimental set-up*

The experiments were carried out in a blowing sand wind tunnel in the University of Aarhus. The working section of the tunnel is 15 m long and has a rectangular cross-section of width 0.60 m and height 0.90 m. The wind velocity can be varied between zero and 20 m s^{-1}. The bed is covered with a 25 mm thick layer of uniform sand grains. A sketch of the tunnel configuration is shown in figure 1. A small bell mouth, followed by turbulence spires and a 3 m long replaceable array of roughness blocks, provides a turbulent boundary layer with the same effective roughness as that induced by ongoing saltation in the main part of the working section. Grains are fed into the tunnel 1 m before the end of the roughness array and caught in a 4 m wide expansion (sand collector) before an axial fan at the end of the tunnel.

2.2. *Experimental procedure*

A set of experiments were carried out using sieved sand grains having a median diameter $\hat{d} = 242$ µm and $\hat{\rho}_p = 2500$ kg m^{-3}. The wind speed was varied from the threshold of sand transport up to a friction velocity of 0.67 m s^{-1} (see table 1).

Before each run, the sand bed was flattened. Each run lasted several minutes in order to accomplish several measurements. The air velocity profile, the grain velocity profile and the grain concentration profile were simultaneously measured. In addition, at the end of each experiment, the sand collected in the expansion box of the wind tunnel was weighed and a height-integrated sand flux $\hat{Q}$ per unit width calculated (see table 1).

2.3. *Air velocity measurements*

The wind velocity was measured at different heights from 2 cm to 20 cm above the sand bed by means of Pitot tubes for the different runs. Note that for all the runs, fully developed, steady saltation was reached. The accuracy of these measurements was about 5 %. The wind profile was well approximated by the classical logarithmic law for turbulent boundary layers:

$$\hat{U} = \frac{\hat{u}^*}{\kappa} \ln\left(\frac{\hat{y}}{\hat{y}_0}\right), \tag{2.1}$$

where $\hat{u}^*$ is the friction velocity; κ is the von Kármán constant ($\kappa = 0.41$); and $\hat{y}_0$ is the aerodynamic roughness. The roughness was found to vary with the friction velocity and could be well fit by the Bagnold roughness law:

$$\hat{y}_0 = \hat{y}_f \exp\left(\frac{-\kappa\, \hat{u}_f}{\hat{u}^*}\right), \tag{2.2}$$

where $\hat{y}_f$ is the height of the focus point and $\hat{u}_f$ is the corresponding wind velocity ($\hat{y}_f = 5.6$ mm and $\hat{u}_f = 3$ m s^{-1}). The existence of the focus was predicted by Bagnold (1941); it results from the drag of the particles slowing the mean gas velocity near the bed. Associated with this is a decrease in the fluid shear stress at the bed with increasing wind speed (Ptasinski *et al.* 2003)

2.4. *Particle velocity and concentration measurements*

The grain velocity profile was obtained by means of PIV and PTV. These velocimetry techniques are non-intrusive measurements and are widely used for determining the velocity field in a fluid (gas or liquid). Here, they were employed to measure the velocity field of the saltating particles. A high-powered pulsed laser served as the light source for generating a vertical laser sheet (see figure 1). Particles passing within the light sheet were illuminated, and a digital camera was able to capture each light pulse in separate image frames.

In the PIV procedure, once a sequence of two light pulses is recorded, the images are divided into small subsections called interrogation areas. The interrogation areas from each image frame are cross-correlated with each other, pixel by pixel. The correlation produces a signal peak, identifying the common particle displacement. A velocity vector map over the whole target area is obtained by repeating the cross-correlation for each interrogation area over the two image frames captured by the camera. In complex particulate flows, which exhibit a large range of particle velocities, the dynamic range of the standard PIV method is often saturated, and severe limitations occur on the measurability of some flow quantities. This is the case for the flow of saltating particles, where there exists a great heterogeneity of the particle velocities due to the existence of two distinct populations of grains: the ascending grains and the descending ones.

An alternative technique, which allows these limitations to be circumvented, is PTV. With this technique, the evaluation of the particle displacement is performed by individual particle tracking, not by means of spatial correlation. This technique allows, in particular, the distinction between ascending and descending particles and the calculation of their respective mean velocity fields. A comparison of the two types of measurements is shown in figure 2. We provide, in addition, LDA data that can be taken as reference measurements. Indeed, the resolution of the velocity of an individual particle with this optical method is ±0.05 m s^{-1}, which is much better than the accuracy obtained with image velocimetry (±0.2 m s^{-1}). The PTV data agree very

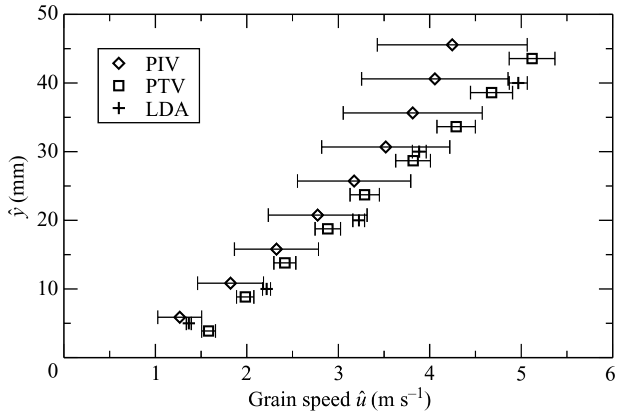

FIGURE 2. Grain velocity profile: comparison between PTV, PIV and LDA: $\hat{u}^* = 0.56$ m s^{-1}.

well with the LDA data, whereas the PIV data deviate from the LDA data, and the deviation increases with increasing altitude. At $\hat{y} = 50$ mm, the PIV measurements underestimate the grain velocity by 20 %. The reason for this discrepancy comes from the fact that as the distance from the bed increases, the velocity difference between the ascending and descending particles increases, and in this situation, the PIV method fails due to the heterogeneity of the particle velocity.

The particle concentration profile can be extracted from the images by means of particle counting. An image is divided into successive horizontal layers of height $\hat{h} = 5$ mm, and in each layer i, the number of particles N_i is determined. The corresponding particle concentration $\hat{n}_i$ is then calculated: $\hat{n}_i = N_i/(\hat{W}\,\hat{L}\,\hat{h})$, where $\hat{L}$ is the horizontal size of the images and $\hat{W}$ is the width of the laser sheet. Alternatively, the particle volume fraction ν can be determined: $\nu = (\pi/6)\hat{d}^3\,\hat{n}$. To get reasonable statistics, the particle concentration profile is averaged over several hundreds of images.

3. Experimental results

3.1. *Particle concentration profile*

Vertical profiles of particle concentration for various friction velocities are shown in figure 3. The vertical height is denoted by $\hat{y}$ and is measured from the surface of the sand bed. At a given shear velocity, the particle volume fraction, ν, was found to decrease with height at an exponential rate:

$$\nu(\hat{y}) = \nu_0 \exp(-\hat{y}/\hat{l}_\nu), \tag{3.1}$$

where ν_0 is the particle volume fraction extrapolated to the bed (i.e. $\hat{y} = 0$) and $\hat{l}_\nu$ is the characteristic decay height. First, it is important to note that the particle volume fraction was estimated from particle counting. Consequently, the calculation requires the accurate determination of the volume of measure, which is closely related to the width $\hat{W}$ of the laser sheet within about one or two grain diameters. This width is equal to 2 mm or, equivalently, eight grain diameters. Consequently, the estimated relative error due to the uncertainties of the volume measure can be as large as 25 %. This error represents a systematic bias and not random fluctuations. Second, data were not obtained close to the bed (i.e. for $\hat{y} < 5$ mm), because the particle density there was too high, and it was difficult to properly enumerate all of the grains.

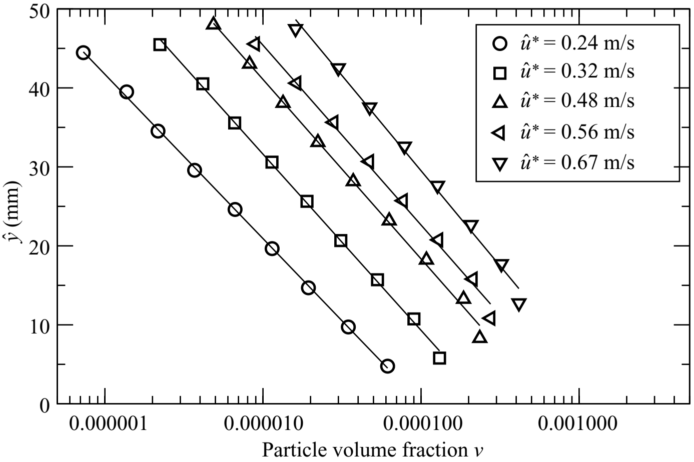

FIGURE 3. Variation of the particle volume fraction versus the vertical height $\hat{y}$ for different friction velocities in a log-linear plot: the solid lines correspond to exponential fits.

Two important features can be extracted from the data. The first is the independence of the decay height on the friction velocity (see figure 4*a*): $\hat{l}_\nu \approx 40\hat{d} \pm 2\,\hat{d}$. The second is the variation of the volume fraction as a function of the friction velocity. As the air velocity increases, the particle concentration is enhanced: the fluid has a higher momentum and is capable of transporting more particles. Therefore, the particle concentration extrapolated to the bed increases with increasing friction velocity (see figure 4*b*). At the first order, the concentration increase can be represented as being proportional to the Shields parameter S^*:

$$\nu_0 = \beta\,(S^* - S_c), \tag{3.2}$$

with $\beta \approx 0.017$ and $S_c \approx 0.009$, where S_c is the critical Shields parameter below which saltation can not be sustained.

3.2. *Particle velocity profile*

Figure 5 shows the variation of the mean horizontal particle velocity as a function of the vertical height for various friction velocities. The particle velocity profile greatly differs from the air velocity profile; the particle velocity is, indeed, found to vary almost linearly with the height. This result contrasts with that found by Yang *et al.* (2007). They showed using PIV measurements that the grain velocity profile scales as $\hat{u} \sim \sqrt{\hat{y}}$. This discrepancy comes from the fact that the PIV technique, as shown in the previous section, underestimates the grain speed due the heterogeneity of the grain velocity field.

Because the airflow provides the driving force for particle motion, it is not surprising that the particle velocity increases with increasing friction velocity. It is interesting to see that all profiles converge towards a speed of about 1 m s^{-1} at the bed. This value can be interpreted as the slip velocity of the particles at the bed. It is also instructive to calculate the relative particle velocity and compare it with that of the air as a function of the height (see figure 6). The relative particle velocity profiles fall on parallel straight lines:

$$\frac{\hat{U} - \hat{u}}{\hat{U}} = \delta - \frac{\hat{y}}{\gamma \hat{d}}, \tag{3.3}$$

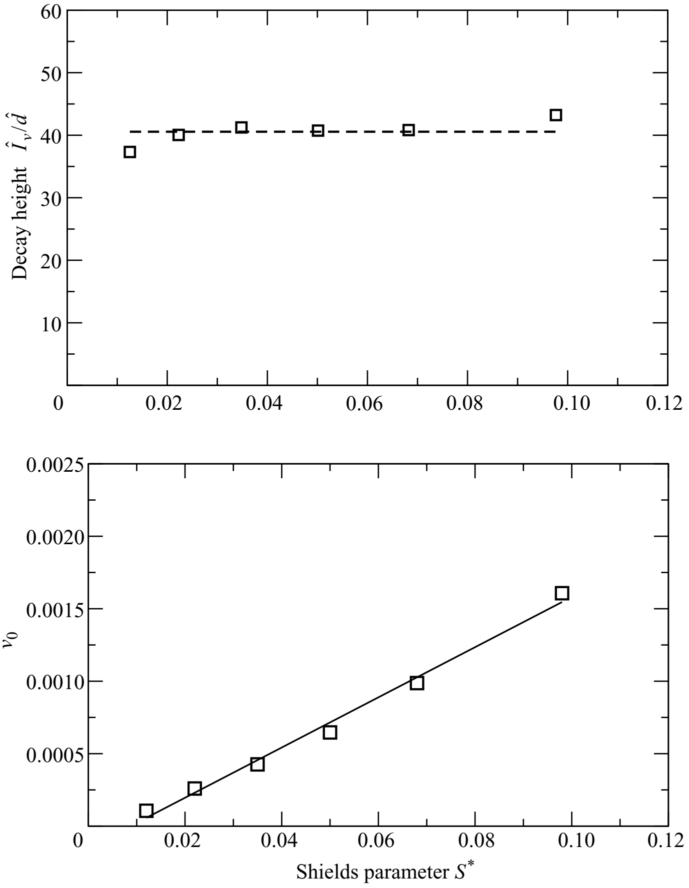

FIGURE 4. (*a*) Dimensionless decay height $\hat{l}\nu/\hat{d}$ versus the Shields parameter S^*; (*b*) particle volume fraction at the bed versus the Shields parameter.

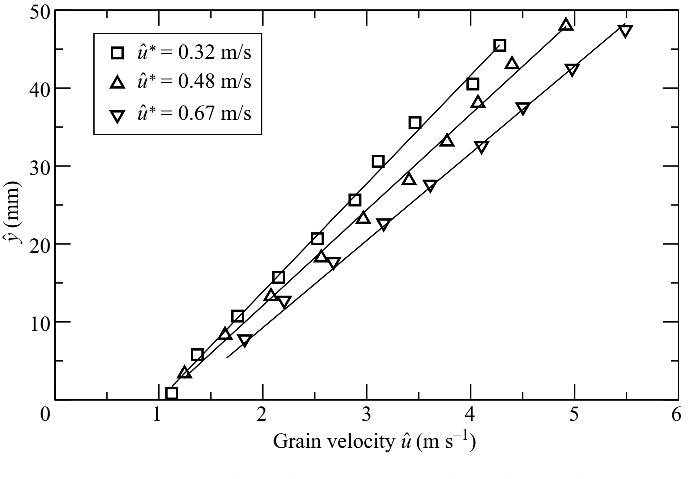

FIGURE 5. Mean horizontal particle velocity versus height for various friction velocities.

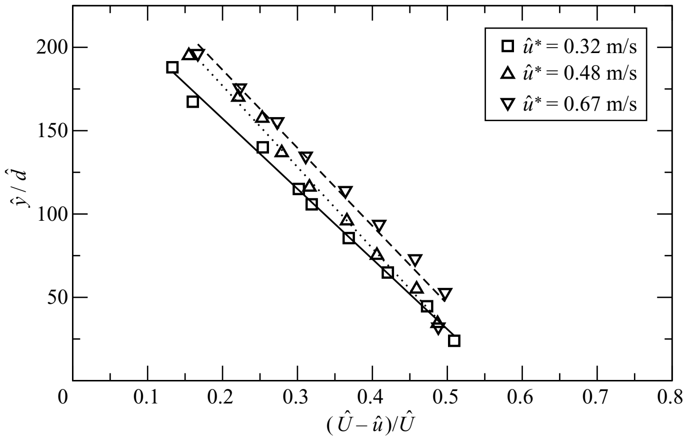

FIGURE 6. Relative particle velocity versus height for various friction velocities.

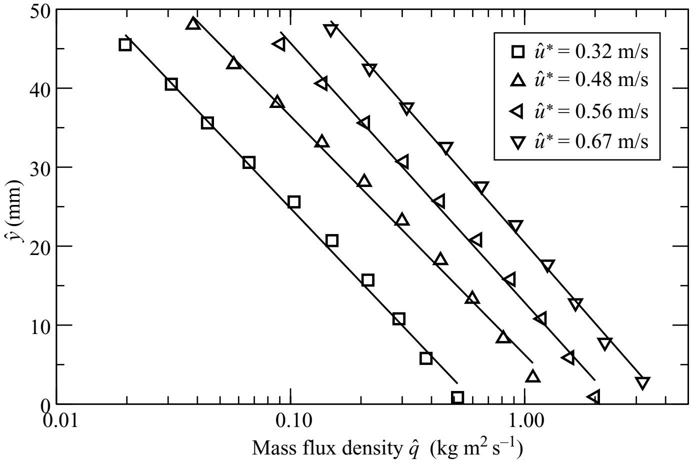

FIGURE 7. Mass flux density profiles for different friction velocities.

where δ and γ are fitting parameters. The parameter δ varies from 0.55 to 0.6 with increasing friction velocity and γ is, more and less, independent of it ($\gamma \approx 500$). The higher the grains are, the faster they flow. The extrapolation of (3.3) to greater heights reveals that the grain velocity would reach the air velocity at the height $\hat{y} \approx 300\,\hat{d}$.

3.3. *Mass flow rate profile*

The local mass flux density is

$$\hat{q}(\hat{y}) = \hat{\rho}_p\, \nu(\hat{y})\, \hat{u}(\hat{y}). \tag{3.4}$$

Therefore, it can easily be computed from the concentration and particle velocity profiles. The result is shown in figure 7. The flux density decreases with increasing height at an exponential rate ($\hat{q}(\hat{y}) = \hat{q}_0 \exp(-\hat{y}/\hat{l}_q)$), like the particle concentration. It means that the vertical variation of the flux density is essentially driven by the particle concentration. In addition, we find that the characteristic decay length $\hat{l}_q$ of the flux density is independent of the friction velocity and that $\hat{l}_q \approx \hat{l}_\nu$.

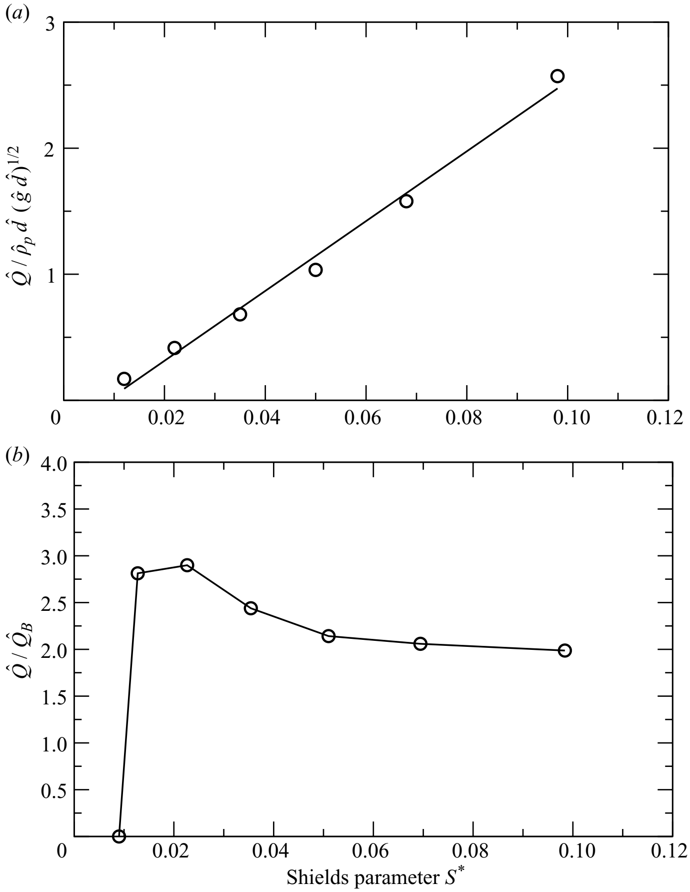

FIGURE 8. (*a*) Dimensionless mass flow rate $\hat{Q}/(\hat{\rho}_p\hat{d}\sqrt{\hat{g}\hat{d}})$ as a function of the Shields parameter. (*b*) Mass flow rate, rescaled by the Bagnold rate $\hat{Q}_B=(\hat{\rho}_p/\hat{g})\hat{u}^{*3}$, as a function of S^*.

From the flux density profiles, we can calculate the mass flow rate $\hat{Q}$, which is the height-integrated flux density: $\hat{Q}=\hat{\rho}_p\int_0^\infty d\hat{y}\;\nu(\hat{y})\,\hat{u}(\hat{y})$. We find that the mass flow rate varies linearly with the Shields parameter, as shown in figure 8:

$$\frac{\hat{Q}}{\hat{\rho}_p\,\hat{d}\,\sqrt{\hat{g}\hat{d}}}\approx\chi\,(S^*-S_c),\tag{3.5}$$

with $\chi\approx 28$ and $S_c\approx 0.009$. We can rewrite (3.5) in terms of the friction velocity, $\hat{u}^*$:

$$\hat{Q}\approx\frac{\chi\hat{\rho}_f}{\hat{g}}\,\sqrt{gd}\,(\hat{u}^{*2}-\hat{u}_c^{*2}),\tag{3.6}$$

with $\hat{u}_c^*=\sqrt{\hat{\rho}_p\hat{g}\hat{d}\;S_c/\hat{\rho}_f}\approx 0.20$. This law exhibits a peak when expressed as $\hat{Q}/\hat{u}^{*3}$ versus $\hat{u}^*$ (see figure 8*b*) and is similar to that proposed by Ungar & Haff (1987). It is also compatible with that derived more recently by Sørensen (2004). However, (3.6) is different from the formulae proposed by Kind (1976) and Owen (1980) (i.e. $\hat{Q}\sim\hat{u}^*(\hat{u}^{*2}-\hat{u}_c^{*2})$), which do not exhibit a maximum for $\hat{Q}/\hat{u}^{*3}$.

4. Theoretical description

4.1. *Model equations*

The theory is phrased in terms of dimensionless variables. Lengths are made dimensionless by $\hat{d}$; velocities are made dimensionless by $\sqrt{\hat{g}\hat{d}}$; and stresses are made dimensionless by $\hat{\rho}_p\hat{g}\hat{d}$.

4.1.1. *Gas phase*

The dimensionless shear stress S in the gas phase is given by

$$S = \mu^T \frac{\mathrm{d}U}{\mathrm{d}y}, \tag{4.1}$$

where μ^T is the dimensionless eddy viscosity,

$$\mu^T = \sqrt{\frac{S}{\sigma}}\kappa y, \tag{4.2}$$

with $\sigma = \hat{\rho}_p/\hat{\rho}_f$, where $\hat{\rho}_p$ and $\hat{\rho}_f$ are respectively the particle and fluid densities.

4.1.2. *Grain phase*

Neglecting collisions between particles within the flow, the dimensionless shear stress s in the particle phase is solely due to kinetic contributions:

$$s = -\nu\langle\xi_x\xi_y\rangle, \tag{4.3}$$

where $\boldsymbol{\xi} = (\xi_x, \xi_y)$ is the velocity of an individual particle and $\langle\,.\,\rangle$ denotes an average over all particles at a given height. The determination of the particle shear stress can be estimated from a determination of the particle trajectories and a knowledge of the particle velocity distribution at the bed.

The trajectories of the grains are determined by

$$\frac{\mathrm{d}\boldsymbol{x}}{\mathrm{d}t} = \boldsymbol{\xi}, \tag{4.4}$$

$$\frac{\mathrm{d}\boldsymbol{\xi}}{\mathrm{d}t} = -\boldsymbol{e}_y + \frac{\mathscr{C}}{\sigma}(U - \xi_x)\boldsymbol{e}_x, \tag{4.5}$$

where $\mathscr{C}$ is the dimensionless drag coefficient, given by

$$\mathscr{C} = 0.3\sqrt{(U - \xi_x)^2 + \xi_y^2} + 18/Re, \tag{4.6}$$

in which Re is a Reynolds number:

$$Re = \frac{\hat{\rho}_f\hat{d}\sqrt{\hat{g}\hat{d}}}{\hat{\mu}_f}. \tag{4.7}$$

Note that the drag on the grains in the vertical direction is taken to be negligible compared to gravity.

The particle velocity distribution is not known *a priori*. We assume a half-Gaussian distribution at the bed for the ascending particles in a two-dimensional approximation:

$$f_\uparrow = \frac{2n_{0\uparrow}}{2\pi\sqrt{T_{x\uparrow}T_{y\uparrow}}}\mathrm{e}^{-(\xi_{0x}-u_{0\uparrow})^2/2T_{x\uparrow}}\mathrm{e}^{-\xi_{0y}^2/2T_{y\uparrow}}, \tag{4.8}$$

where $n_{0\uparrow}$ is the number density of ascending particles made dimensionless by d^3; $u_{0\uparrow}$ is the dimensionless mean horizontal slip velocity of the ascending particles;

and $T_{x\uparrow} = \langle \xi_{0x}^2 \rangle_\uparrow$ and $T_{y\uparrow} = \langle \xi_{0y}^2 \rangle_\uparrow$ respectively are the dimensionless variances of the horizontal and vertical velocity distributions (i.e. the so-called granular temperature).

Several important observations follow: (i) Because the vertical drag on the particles is neglected, the distribution of the vertical velocities for the ascending and descending particles should be identical. Consequently, $2n_\uparrow = 2n_\downarrow = n$ and $T_{y\uparrow} = T_{y\downarrow} = T_y$ at any altitude y. (ii) For the same reason, it can be shown (see Appendix A) that the vertical velocity distribution remains half-Gaussian at any dimensionless height y, with a uniform velocity fluctuation T_y, and that

$$n(y) = n_0\, \mathrm{e}^{-y/T_y}. \tag{4.9}$$

(iii) In contrast, nothing can be said *a priori* about the horizontal velocity distribution of the descending particles at the bed. However, it will be assumed to be a half-Gaussian distribution, as well:

$$f_\downarrow = \frac{2n_0}{2\pi\sqrt{T_{x\downarrow} T_y}} \mathrm{e}^{-(\xi_{0x} - u_{0\downarrow})^2/2T_{x\downarrow}} \mathrm{e}^{-\xi_{0y}^2/2T_y}, \tag{4.10}$$

with a slip velocity $u_{0\downarrow}$ different from $u_{0\uparrow}$. This difference of slip velocities is associated with the non-zero particle shear stress at the bed. Indeed, the particle shear stress s_0 at the bed is given by $s_0 = \nu_0 \sqrt{T_y/2\pi}(u_{0\downarrow} - u_{0\uparrow})$, where the volume fraction ν_0 is simply related to the dimensionless number density $n_0 = (6/\pi)\nu_0$.

Finally, because the total shear stress is constant through the depth of the flow, $S = S^* - s$, where S^* is the dimensionless shear stress in the particle-free gas – the Shields parameter.

4.1.3. *Boundary conditions at the bed*

At the bed, complex collision processes take place. Saltating particles are accelerated by the gas flow and are driven downward by gravity to collide at low angles with the bed. Each collision typically produces another high-energy particle leaving the bed at a relatively high angle and several low-energy grains that are impelled forward by the collision into a series of short hops. This collision process can be described via a statistical function that characterizes the relationship between a single incoming grain and the products of the collision. More explicitly, given that a particle with velocity $\boldsymbol{\xi}$ impacts the sand surface, $\mathscr{S}(\boldsymbol{\xi} \rightarrow \boldsymbol{\xi}')d\boldsymbol{\xi}'$ is the expected number of particles per unit volume that leave the surface with velocity around $\boldsymbol{\xi}'$; $\mathscr{S}(\boldsymbol{\xi} \rightarrow \boldsymbol{\xi}')$ is called the splash function.

The first velocity moment of the splash function has been measured experimentally with beads of a few millimetres in diameter (Beladjine *et al.* 2007). Numerical simulations phrased in terms of dimensionless variables are able to reproduce the results of the experiment (Oger *et al.* 2005), indicating that the experiments on large beads can be used to provide boundary conditions for particles as small as those of sand. However, the spheres and the sand may differ in their coefficients of restitution and friction.

In principle, knowledge of the splash function permits the derivation of the ascending velocity distribution at the bed $f_\uparrow$ as a function of the descending velocity distribution $f_\downarrow$. Here, the aim is only to discuss the first moments of these distributions, consistent with the available experimental data on the splash function. It is, therefore, legitimate to assume that both velocity distributions are half-Gaussian (see (4.8) and (4.10)). As previously discussed, $n_{0\uparrow} = n_{0\downarrow} = n_0/2$ and $T_{y\uparrow} = T_{y\downarrow} = T$, but *a priori* $u_{0\uparrow} \neq u_{0\downarrow}$. In addition, the horizontal and vertical velocity fluctuations are assumed to be identical: $T_{x\downarrow} = T_{y\downarrow} = T$. Following the procedure used by Richman (1988), we will deduce the value of T, $u_{0\downarrow}$ and $u_{0\uparrow}$ from the splash function, as well as a relation between the number density at the bed n_0 and the particle shear stress at the ground s_0. Then, in the model outlined above for the dynamics of a distribution of grains, the only parameter that remains to be determined is the number density at the bed n_0 (or equivalently the solid volume fraction $\nu_0 = (\pi/6)\, n_0$).

4.2. *Derivation of the boundary conditions*

4.2.1. *Experimental splash function*

The impact of a grain on a bed usually generates one high-energy particle called the 'rebound' particle plus a number of lower energy particles called the 'ejecta' (Anderson, Sørensen & Willetts 1991). The splash function is thus usually expressed as the sum of two contributions $\mathscr{S} = \mathscr{S}_R + \mathscr{S}_E$ referring, respectively, to the rebound and the ejecta.

The phenomenological laws for the number of ejected particles and for the restitution coefficients, given in the paper by Beladjine *et al.* (2007), will be used as input data. They are related to the splash functions $\mathscr{S}_R$ and $\mathscr{S}_E$ through the integral expressions given below. The restitution coefficient e (respectively, e_y) is the ratio between the impinging particle velocity (respectively, vertical velocity) and the averaged velocity ξ'_r (respectively, vertical velocity ξ'_{yr}) after rebound. They are well fit by the following relations:

$$e(\boldsymbol{\xi}) = 1/\xi \int_{\xi'_y>0} \xi' \mathscr{S}_R(\xi \rightarrow \xi')\mathrm{d}\boldsymbol{\xi}' \approx A - B\sin\theta, \tag{4.11}$$

$$e_y(\boldsymbol{\xi}) = 1/|\xi_y| \int_{\xi'_y>0} \xi'_y \mathscr{S}_R(\xi \rightarrow \xi')\mathrm{d}\boldsymbol{\xi}' \approx \frac{A_y}{\sin\theta} - B_y, \tag{4.12}$$

with $\xi_y = -\xi\sin\theta$ (see figure 16) and $A = 0.87$, $B = 0.72$, $A_y = 0.30$ and $B_y = 0.15$. These quantities depend on the coefficients of restitution and friction of the grains (Oger *et al.* 2005).

The number of ejected particles is

$$N_{ej}(\boldsymbol{\xi}) = \int_{\xi'_y>0} \mathscr{S}_E(\xi \rightarrow \xi')\mathrm{d}\boldsymbol{\xi}' = N_0(1-e^2)\left(\frac{\xi}{\xi_0} - 1\right) \tag{4.13}$$

with $N_0 = 13$ and $\xi_0 = 40$. The quantity ξ_0 represents the velocity threshold below which there is no ejection.

Finally, the experimental cutoff for the velocity is $\xi_c = \sqrt{2}$, and particles ejected or re-ejected with a smaller velocity are not recorded. The impact velocities investigated in the experiment are mainly larger than the velocity threshold for ejection ξ_0. The restitution coefficients for $\xi \ll \xi_0$ are, thus, extrapolated values.

4.2.2. *Determination of the fluxes at the bed*

General method. The flux of beads impacting the bed is directly related to the flux of beads leaving the bed. The definition of the splash function implies the following boundary condition for f at a point on a wall with upward unit normal $\boldsymbol{n}$ (Cercignani 1988):

$$|\boldsymbol{\xi}' \cdot \boldsymbol{n}| f(\boldsymbol{\xi}') = \int_{\boldsymbol{\xi}\cdot\boldsymbol{n}<0} \mathscr{S}(\xi \rightarrow \boldsymbol{\xi}') f(\boldsymbol{\xi}) |\boldsymbol{\xi}\cdot\boldsymbol{n}| \mathrm{d}\boldsymbol{\xi} \qquad (\boldsymbol{\xi}'\cdot\boldsymbol{n} > 0), \tag{4.14}$$

where the time and space dependencies have been omitted, because the flow is assumed to be steady and fully developed over a flat surface.

The average vertical flux of a quantity φ is

$$n\langle\varphi\xi_y\rangle = \int \varphi(\boldsymbol{\xi})\xi_y f(\boldsymbol{\xi})\mathrm{d}\boldsymbol{\xi}, \tag{4.15}$$

where y is the dimensionless vertical coordinate. Using 4.14, with n the dimensionless number of particles per unit volume

$$\begin{aligned} n\langle\varphi\xi_y\rangle &= \int_{\xi_y>0} \varphi(\boldsymbol{\xi})\xi_y f(\boldsymbol{\xi})\mathrm{d}\boldsymbol{\xi} + \int_{\xi_y<0} \varphi(\boldsymbol{\xi})\xi_y f(\boldsymbol{\xi})d\boldsymbol{\xi} \\ &= \int_{\xi_y>0} \varphi(\boldsymbol{\xi}) \int_{\xi'_y<0} \mathscr{S}(\boldsymbol{\xi}' \rightarrow \boldsymbol{\xi}) f(\boldsymbol{\xi}')|\xi'_y|\mathrm{d}\boldsymbol{\xi}'\,\mathrm{d}\boldsymbol{\xi} \\ &\quad + \int_{\xi_y<0} \varphi(\boldsymbol{\xi})\xi_y f(\boldsymbol{\xi})\mathrm{d}\boldsymbol{\xi}. \end{aligned}$$

By exchanging the labels $\boldsymbol{\xi}$ and $\boldsymbol{\xi}'$ in the first term, the complete expression can be reduced to

$$n\langle\varphi\xi_y\rangle = \int_{\xi_y<0} f(\boldsymbol{\xi})|\xi_y| \left[\int_{\xi'_y>0} \mathscr{S}(\boldsymbol{\xi} \rightarrow \boldsymbol{\xi}')\varphi(\boldsymbol{\xi}')\mathrm{d}\boldsymbol{\xi}' - \varphi(\boldsymbol{\xi})\right] \mathrm{d}\boldsymbol{\xi}. \tag{4.16}$$

Equation 4.16 is the basic expression from which the boundary conditions are derived by using successively $\varphi = 1$, $\varphi = \xi_x$ and $\varphi = \xi_y$. It does not involve the velocity distribution for $\boldsymbol{\xi}'$.

Particle flux. The particles ejected with a very low velocity are not recorded, and only the particles with a velocity larger than $\xi_c = \sqrt{2}$ are taken into account to define the number of ejected particles. Note that $\sqrt{2}$ corresponds to the dimensionless ejection velocity for a particle to reach a height equal to its diameter. So, by definition, $\mathscr{S}_E(\boldsymbol{\xi} \rightarrow \boldsymbol{\xi}') = 0$ if $\xi' < \xi_c$. Consistently, the particles rebounding with an average velocity ξ'_r smaller than ξ_c will be considered as lost – i.e. $\int \mathrm{d}\boldsymbol{\xi}'\mathscr{S}_R(\boldsymbol{\xi} \rightarrow \boldsymbol{\xi}') = 0$, if $\xi'_r < \xi_c$ (or, equivalently, $\xi < \xi_c/e$), and $= 1$ otherwise.

In a fully developed, steady flow, the net particle flux vanishes and the amount of ejected grains per unit time, exactly Φ_{ej}, balances the amount of impacting grains trapped by the bed, Φ_{loss} (c.f. (4.16) with $\varphi = 1$).

The vertical flux of ejected particles is

$$\Phi_{ej} = \int_{\xi_y<0,\xi>\xi_0} f(\boldsymbol{\xi})N_{ej}(\boldsymbol{\xi})|\xi_y|\mathrm{d}\boldsymbol{\xi} \tag{4.17}$$

with f given by (4.10) and N_{ej} by (4.13). The cutoff velocity ξ_0 is larger than the average velocity of the grains, as will be checked *a posteriori*. Therefore, the main contribution to the integral comes from velocities very close to $(\xi_0, 0)$, as shown in figure 16. An expansion around $\boldsymbol{\xi} = (\xi_0, 0)$ and $\theta = 0$, detailed in Appendix B, leads to

$$\Phi_{ej} \approx \frac{n_0 N_0}{2\pi T} \frac{T^3}{u_{0\downarrow}(\xi_0 - u_{0\downarrow})^2} \mathrm{e}^{-(\xi_0 - u_{0\downarrow})^2/2T} \left(1 - A^2 + AB\sqrt{\frac{2\pi T}{\xi_0 u_{0\downarrow}}}\right). \tag{4.18}$$

The number of beads trapped by the bed per unit time and per unit surface is given by

$$\Phi_{loss} = \int_{\xi_y<0,\xi'_r<\xi_c} f(\boldsymbol{\xi})|\xi_y|\mathrm{d}\boldsymbol{\xi}. \tag{4.19}$$

The region of integration is a small domain around $\xi = 0$, and the integral is performed assuming a constant density in this domain (i.e. $f(\boldsymbol{\xi}) \approx f(0,0)$). Thus (see Appendix C),

$$\Phi_{loss} \approx 74\,\frac{n_0}{2\pi T}\,\xi_c^3 \mathrm{e}^{-u_{0\downarrow}^2/(2T)}. \tag{4.20}$$

Equality of both particles fluxes ($\Phi_{ej} = \Phi_{loss}$) yields

$$74\,\xi_c^3 = N_0\,\frac{T^3}{u_{0\downarrow}(\xi_0 - u_{0\downarrow})^2}\,\mathrm{e}^{-\xi_0^2/(2T)}\,\mathrm{e}^{u_{0\downarrow}\xi_0/T}\left(1 - A^2 + AB\sqrt{\frac{2\pi T}{\xi_0 u}}\right). \tag{4.21}$$

Horizontal momentum flux. The horizontal velocity of an impacting particle is reduced during the collision, leading to a momentum transfer to the bed or, equivalently, a positive shear stress. Only a very small number of collisions lead to ejected beads, and the mean horizontal velocity of these ejected bead is very small (of the order of unity). The momentum transfer is thus dominated by the rebound properties of the colliding beads; the momentum of the ejected beads will be shown to be fully negligible. The dimensionless shear stress, s_0, at the bed is thus given by

$$\begin{aligned} s_0 &= -m\int_{\xi_y<0} f(\boldsymbol{\xi})|\xi_y|\left[\int_{\xi_y'>0}\mathscr{S}_R(\boldsymbol{\xi}\to\boldsymbol{\xi}')\xi_x'\mathrm{d}\boldsymbol{\xi}' - \xi_x\right]\mathrm{d}\boldsymbol{\xi} \\ &= m\int_{\xi_y<0} f(\boldsymbol{\xi})|\xi_y|(\xi_x - \xi_{x,r}')\mathrm{d}\xi_x\mathrm{d}\xi_y, \end{aligned} \tag{4.22}$$

where the parameter $m = \pi/6$ is the dimensionless bead mass.

As detailed in Appendix D, the integral is well approximated by

$$s_0 \approx \nu_0 T\left[0.5\sqrt{B^2 - B_z^2} + \left(1 - \frac{AB - A_zB_z}{\sqrt{B^2 - B_z^2}}\right)\frac{1}{\sqrt{2\pi}}\frac{u}{\sqrt{T}} + \frac{AB - A_zB_z}{\sqrt{B^2 - B_z^2}}\frac{1}{\sqrt{2\pi}}\frac{\sqrt{T}}{u}\right]. \tag{4.23}$$

Vertical momentum flux. In the same way, the vertical momentum flux, or the pressure, is determined. Here, again, the ejected particles have negligible contribution:

$$\begin{aligned} P &= m\int_{\xi_y<0} f(\boldsymbol{\xi})|\xi_y|(\xi_{y,r}' - \xi_y)\mathrm{d}\boldsymbol{\xi} \\ &= mnT\left[\frac{A_y}{\sqrt{2\pi}}\left(\frac{u_{0\downarrow}}{\sqrt{T}} + \frac{\sqrt{T}}{u_{0\downarrow}}\right) - \frac{B_y}{2}\right] + \frac{mnT}{2}. \end{aligned} \tag{4.24}$$

These two terms are the exact values of the integral involving respectively $\xi_{y,r}'$ and ξ_y. The second term is the expected value of the pressure for a Gaussian velocity distribution, restricted to the impinging particles.

The vertical momentum flux is *a priori* unknown. Nevertheless, if the collisions between grains in the flow and the vertical drag force due to the wind are negligible, the only contribution to P is the kinetic pressure, and with the assumed velocity distribution, the pressure at the bed becomes $P = m(n_{0\downarrow}T_{y\downarrow} + n_{0\uparrow}T_{y\uparrow})$. The relation $n_{0\downarrow} = n_{0\uparrow}$ and $T_{y\downarrow} = T_{y\uparrow} = T$ finally gives $P = mn_0T$.

Using (4.24), this leads to

$$\frac{u_{0\downarrow}}{\sqrt{T}} \approx \frac{\pi}{2}\frac{1 + B_y}{A_y} \tag{4.25}$$

Upon employing the parameters of the splash function determined by Beladjine *et al.* (2007), we obtain $u_{0\downarrow}/\sqrt{T} \approx 4.6$. This relation says, roughly, that the average vertical restitution coefficient is equal to unity, which is required for a steady and fully developed saltation motion. Using (4.12), it can be deduced that the mean impact angle satisfies $\langle \sin\theta \rangle = A_y/(B_y + 1) = 0.26$, leading to $\langle \theta \rangle_{imp} \sim 15°$. As the vertical impacting velocity is roughly $\sqrt{T}$, the approximate relation $u_{0\downarrow} \sim 4\sqrt{T}$, very similar to (4.25), is obtained. The collisions are nevertheless dissipative, and the averaged horizontal restitution coefficient is smaller than unity. The bed converts horizontal momentum into vertical momentum, keeping the grain sheet from collapsing. In a steady, fully developed flow, the lost horizontal momentum is recovered from the wind.

Determination of $u_{0\downarrow}$, T *and* n_0. Upon employing (4.25) in (4.21) and (4.23), the values of $u_{0\downarrow}$ and T can be deduced as functions of the parameters A, B, A_y, B_y, ξ_c and ξ_0 of the splash function and an expression for n_0, as a function of the particle shear stress at the bed, obtained. With the parameters of the splash function determined by Beladjine *et al.* (2007)

$$u_{0\downarrow} \approx 20, \quad T \approx 20, \quad \frac{s_0}{\nu_0 T} \approx 0.6. \tag{4.26}$$

The particle shear stress at the bed is related to the difference of slip velocities: $s_0 = \nu_0\sqrt{T/2\pi}(u_{0\downarrow} - u_{0\uparrow})$, so that $u_{0\uparrow} = 0.68u_{0\downarrow} \approx 15$. Replacing the two half-Gaussian distributions $f_\uparrow$ and $f_\downarrow$ used in this paper by a full Gaussian distribution based on the average slip velocity would, thus, only induce an additional error of the order of 25 %.

To check the validity of the approximation used to compute the flux integrals, it is assumed that the particle shear stress at the bed is of the order of the total shear stress S^*. The relative error made in this is less than 20 %. The amount of ejected beads per unit time and surface is $[74\,S^*/(1.2\pi T^2)]\,\xi_c^3 \mathrm{e}^{-u_{0\downarrow}^2/(2T)} \sim 3 \times 10^{-7}$, for $S^* = 0.1$. Experimental results show that the mean vertical velocity of the ejected beads is about three, leading to a flux of vertical velocity of the order of 10^{-6}. This is, indeed, completely negligible with respect to the pressure $P = mn_0T \sim 0.1$, as expected. The contribution to the shear stress of the ejected particle is even smaller.

4.2.3. *Sensitivity of the boundary conditions on the parameters of the Splash function*

As previously mentioned, the values of the parameters A, B, A_y, B_y, N_0 and ξ_0 of the splash function depend on the coefficients of restitution and the friction of grains. It is therefore instructive to investigate how the boundary conditions are modified when these parameters are slightly changed.

We recall that the boundary conditions were derived from mass and momentum balance at the bed (see 4.21, 4.25, 4.23). These conditions fix the values of the temperature T, the descending grain velocity $u_{0\downarrow}$ at the bed and the ratio (denoted later by μ) of the grain shear stress s_0 at the bed to the product of the particle concentration ν_0 and the temperature T. Our purpose here is to determine how sensitive these values are to the parameters of the splash function.

Instead of using numerics to perform this parametric study, it is possible to derive analytical expressions for T, $u_{0\downarrow}$, μ as functions of the parameters of the Splash function, after making some additional reasonable approximations. Assuming that $u_{0\downarrow}/\sqrt{T} \gg 1$, the mass balance (cf. 4.21) reduces to

$$u_{0\downarrow} \approx \frac{\xi_0}{2}, \tag{4.27}$$

which combined with the vertical momentum balance at the bed (cf. 4.25) yields

$$T \approx \frac{A_y^2 \xi_0^2}{2\pi (B_y + 1)^2}. \tag{4.28}$$

Using these in the horizontal momentum balance (cf. 4.23), we obtain

$$\mu = \frac{s_0}{\nu_0 T} \approx \left[0.5\sqrt{B^2 - B_y^2} + \left(1 - \frac{AB - A_y B_y}{\sqrt{B^2 - B_y^2}}\right) \frac{1 + B_y}{2A_y} \right]. \tag{4.29}$$

In light of these calculations, we note first that the particle velocity $u_{0\downarrow}$ is equal to half the impacting velocity threshold ξ_0 below which there is no ejection (see 4.13). Second, the granular temperature T only depends on ξ_0, A_y and B_y and increases with increasing A_y and decreasing B_y. In other words, the granular temperature increases when the vertical restitution coefficient e_y increases or, equivalently, when the transfer of the horizontal momentum to the vertical direction during the rebound is more efficient. Finally, the ratio $\mu = s_0/\nu_0 T$ is found to be a algebraic function of A, B, A_y and B_y. It increases with increasing A_y (or B) and decreasing B_y (or A). It turns out that μ increases when the vertical restitution coefficient e_y increases or when the rebound dissipates more energy (i.e. for decreasing e).

For example, if e_y is decreased, by taking $A_y = 0.45$ and $B_y = 0.3$ (instead of $A_y = 0.30$ and $B_y = 0.15$) and leaving the other parameters unchanged ($A = 88$, $B = 0.73$ and $\xi_0 = 40$), then $u_{0\downarrow} \approx 20$, $T \approx 40$ and $s_0/\nu_0 T \approx 0.075$ (instead of $u_{0\downarrow} \approx 20$, $T \approx 20$ and $s_0/\nu_0 T \approx 0.06$).

4.3. *Numerical simulation*

Numerical simulations have been carried out based on the calculated boundary conditions. These involve the solution of the equations that describe the particle trajectories for a collection of particles with a half-Gaussian distribution of initial velocities, the influence of these particles on the wind and the interaction of the distribution of particles with the bed according to the calculated boundary conditions. The numerical simulation is analogous to that carried out by Werner (1990) but simpler. Werner (1990) employed an experimentally determined splash function and the equations of motion for individual particles interacting with the wind above the bed to calculate the steady velocity distribution function for the upward- and downward-moving particles. The method employed here is simpler because the vertical velocity distributions are assumed to be half-Gaussian, and at the bed, only three low moments of the splash function are employed to relate the unknown parameters of the assumed distributions.

The half-Gaussian velocity distribution of the ascending particles is completely determined by the three parameters $u_{0\uparrow}$, T and ν_0. While the values of $u_{0\uparrow}$ and T are deduced from the boundary conditions, the particle volume fraction ν_0 at the bed is not known *a priori*. A trial value of ν_0 is picked, and a trial logarithmic gas velocity profile is calculated for a flow that is free of particles (i.e. $S = S^*$ for any height y). A set of particles with initial velocities consistent with the specified Gaussian distribution is chosen. The trajectories of the particles from ejection to impact are then calculated using (4.4) and (4.5). This information is used to compute the particle shear stress $s(y)$ (cf. (4.3)), and (4.1) is integrated using $s(y)$ to obtain a new gas velocity profile $U(y)$. The entire cycle is repeated until $U(y)$ converges.

The particle shear stress at the bed, s_0, calculated from the particle trajectories is compared with the value $\mu \nu_0 T$ required by the boundary condition. If, for example,

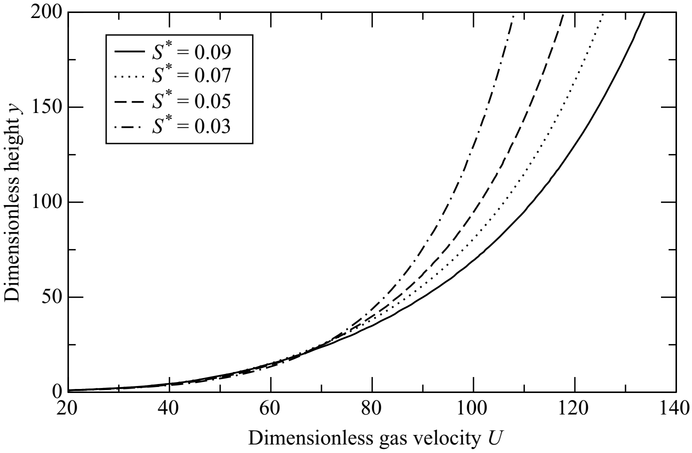

FIGURE 9. Gas velocity profiles (predicted by the simulation) for different Shields parameters. The parameters of the simulation are $u_{0\uparrow} = 20$, $T = 20$ and $\mu = 0.6$.

the calculated quantity is found to be too large, a larger ν_0 is chosen. Note that a larger ν_0 tends to decrease the particle shear stress at the bed. This is not obvious *a priori*, but it is found that $(u_{0\downarrow} - u_{0\uparrow})$ decreases with increasing ν_0 at a nonlinear rate, so that $s_0 = \nu_0\sqrt{T/2\pi}(u_{0\downarrow} - u_{0\uparrow})$ decreases as well. The system of equations is then solved once more. The entire process is repeated until the particle shear stress calculated from the particle trajectories consistent with the required value is found. The whole procedure is implemented in MATLAB. About 10 to 20 iterations are needed for the process to converge with a required error tolerance of 0.001. A family of curves corresponding to different values of the dimensionless shear stress S^* in the particle-free gas is calculated.

4.4. *Simulation results*

For the purpose of comparison with the experimental data, simulations were carried out for a bed of quartz spheres of density $\hat{\rho}_p = 2.5 \times 10^3$ kg m^{-}3 and diameter $\hat{d} = 250$ μm. We first present the general features of the simulation results and examine how sensitive they are on the parameters used for the boundary conditions. Then, we provide a comparison with the experimental data.

4.4.1. *General results and sensitivity on the boundary conditions*

In addition to the Shields parameter, S^*, the simulations depend on the values chosen for the parameters $u_{0\uparrow}$, T and μ. As shown previously, the values of these parameters can be calculated explicitly from the splash function but vary according to the values of the parameters that characterize its first moment. We present below the main features of the results of the simulations and their sensitivity with respect to the values of these parameters.

(i) The gas velocity profiles calculated for different Shields parameters cross at a certain height y_f corresponding to a certain gas velocity u_f (see figure 9). This is the focus predicted by Bagnold (1941). The coordinate values (y_f, u_f) of the focus point are found to depend both on T and μ as follows:

$$y_f \approx 1.2\,T, \tag{4.30}$$

$$u_f \approx 90\,\mu^{0.5}. \tag{4.31}$$

The height of the focus point is directly proportional to the temperature T and is, therefore, closely connected to the mean maximum height reached by the particles ($\bar{h}_{max} = T/2$). The gas speed at the focus height is independent on T but increases with increasing μ.

(ii) The critical Shield parameter, S_c, for incipient transport is found to vary with both T and μ as

$$S_c \approx 0.2\,\mu^{1.5}/\,T^{0.5}.$$

Thus, increasing the temperature decreases the critical Shield parameter.

(iii) The particle shear stress and the grain concentration profiles are both found to be exponential. Their respective dimensionless characteristic decay lengths (l_s and l_ν) are equal to the dimensionless granular temperature T,

$$l_s = l_\nu = T, \tag{4.32}$$

and are insensitive to changes of the Shields parameter, in agreement with the experimental measurements. The simulations indicate, moreover, that over the range of Shields parameter from S_c to 0.2, the variation of the dimensionless particle shear, s_0, and the particle concentration, ν_0, at the bed, can be well captured by the following laws:

$$s_0 \approx S^* - S_c \mathrm{e}^{-\zeta(S*-S_c)} \tag{4.33}$$

and

$$\nu_0 \approx \left[S^* - S_c \mathrm{e}^{-\zeta(S*-S_c)}\right] / (\mu T), \tag{4.34}$$

with $\zeta \approx 0.1 S_c$. The particle shear stress at the bed s_0 increases with increasing Shields parameter and approaches S^* at large Shields parameters at an exponential rate. As a consequence, the fluid shear stress at the bed is not constant, as assumed by Owen (1964), but decays exponentially as $S_c \exp[-\zeta(S^* - S_c)]$. This might be interpreted as a decoupling of the inner wall layer of the gas compared to the outer flow discussed by Hunt, Eames & Westerweel (2006). In case of moderate Shields parameters (i.e. $S^* < 0.1$), (4.33) and (4.34) can be approximated by linear functions of S^*:

$$s_0 \approx 1.1\,(S^* - S_c), \tag{4.35}$$

$$\nu_0 \approx 1.1\,\frac{(S^* - S_c)}{\mu\,T}. \tag{4.36}$$

One can note that the particle concentration ν_0 at the bed increases linearly with the Shield number at a rate given by $1/\mu T$. Increasing the temperature T leads to a decrease of this rate, as illustrated in figure 10.

(iv) The mean grain slip velocity u_0 at the bed is found to vary as

$$u_0 = (u_{0\uparrow} + u_{0\downarrow})/2 \approx u_{0\uparrow} + 0.7\,\mu\,T^{0.5},$$

and the grain velocity profile can be well approximated by a linear profile for $y < 2T$:

$$u(y) \approx u_0 + 2.4\left(\frac{\mu\,S^{*0.2}}{T^{0.5}}\right) y. \tag{4.37}$$

We note that the slope of the grain velocity profiles is weakly sensitive to the Shields parameter and increases linearly with the parameter μ (see figure 11).

(v) The last important result from the simulations is that the mass flux $q(y)$ decreases exponentially with height at the same rate as the particle concentration, confirming that the variation of the mass flux is driven mainly by the particle volume fraction.

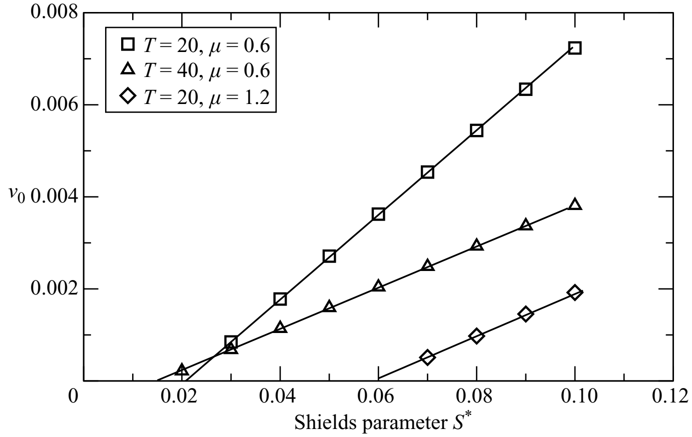

FIGURE 10. Particle volume fraction at the bed, ν_0, versus the Shield number for different values of the model parameters ($u_{0\uparrow} = 20$; $T = 20, 40$; and $\mu = 0.6, 1.2$). Continuous lines correspond to approximate solutions given by (4.34).

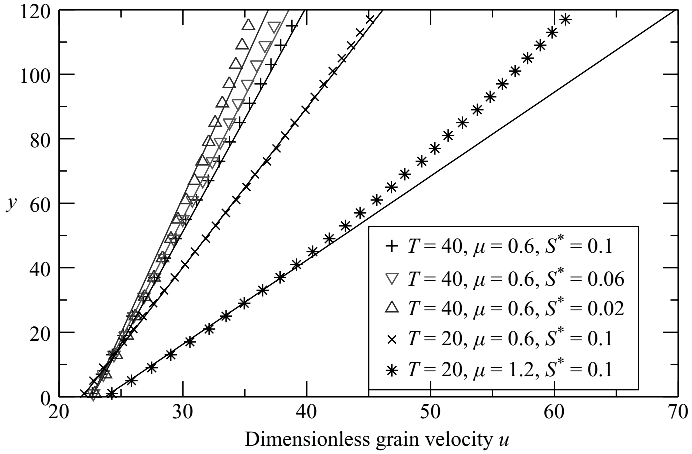

FIGURE 11. Particle velocity profiles for various Shields parameters and different values of the model parameters ($u_{0\uparrow} = 20$; $T = 20, 40$; and $\mu = 0.6, 1.2$). Continuous lines correspond to approximate solutions given by (4.37).

Consequently, the dimensionless height-integrated mass flux Q varies linearly with S^* for moderate Shields parameters and can be well approximated by

$$Q = \int_0^\infty \nu(y)\, u(y)\, \mathrm{d}y \approx \nu_0\, T\, u(T) \approx 1.1 \left(\frac{u_{0\uparrow}}{\mu} + 1.8\, T^{0.5} \right) (S^* - S_c). \tag{4.38}$$

For moderate temperatures, the rate of increase is therefore essentially governed by the ratio $u_{0\uparrow}/\mu$ (see figure 12). It is worthwhile to mention that the simulation indicates that the linearity between the flow rate and the Shields parameter still holds for Shields parameters up to $S^* \approx 0.2$.

4.4.2. *Comparison with the experimental data*

We have just seen that the overall features of the experimental profiles are qualitatively reproduced by the simulations. The remaining important issue is to know

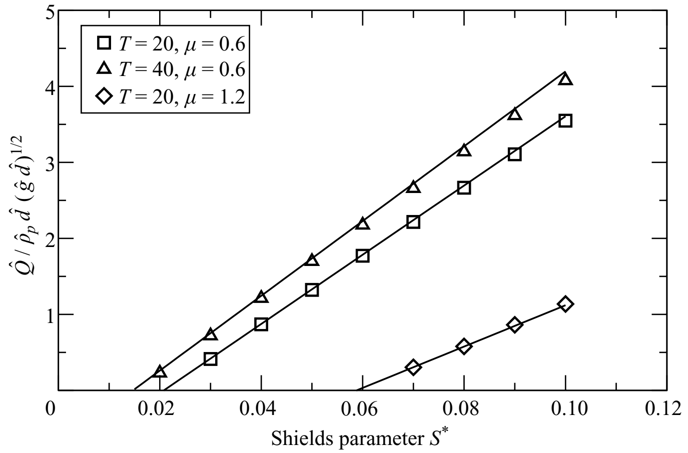

FIGURE 12. Dimensionless particle flux Q versus the Shields parameter for different values of the model parameters ($u_{0\uparrow} = 20$; $T = 20, 40$; and $\mu = 0.6, 1.2$). Continuous lines correspond to approximate solutions given by (4.38).

whether the simulations can provide quantitative predictions. As seen previously, the simulation model depend on three boundary parameters that are intimately connected to the parameters of the splash function, which are not precisely known for the sand grains used for the wind tunnel experiments. As a consequence, we have a certain freedom in the choice of these boundary parameters. The best choice for quantitative agreement with the experimental data is

$$u_{0\uparrow} \approx 15 \text{ (or } u_{0\downarrow} \approx 20), \quad T \approx 40 \quad \text{and} \quad \mu \approx 0.8. \tag{4.39}$$

The first two values were chosen to match respectively the experimental grain slip velocity and the characteristic decay lengths l_v and l_q of the particle concentration and flux profiles. We recall that the model predicts that $l_v = l_q = T$ and $l_v^{exp} = l_q^{exp} \approx 40$. The third value was chosen to match the experimental relation found between the mass flow rate and the Shields parameter. As seen previously, we can infer from these values the corresponding parameters of the splash function.

In figure 13(*a*), we plot the profiles for the gas velocity, obtained with the given values of the model parameters, together with the corresponding experimental profiles. The coordinates of the focus point obtained from the simulations are $\hat{y}_f \approx 1.2 T \hat{d} \approx 12$ mm and $\hat{u}_f \approx 90 \mu^{0.5} \sqrt{gd} \approx 4$ m s^{-1}. The value found for $\hat{u}_f$ is close to the experimental value ($\hat{u}_f^{exp} \approx 3$ m s^{-1}), whereas the predicted focus height is twice that of the experimental estimation ($\hat{y}_f^{exp} \approx 5.6$ mm). We should, however, recall that the experimental measurement of the focus height suffers from a large uncertainty.

Comparison of the grain velocity profiles is shown in figure 13(*b*). The simulations greatly underestimate the slope of the particle velocity profiles. This discrepancy is not explained for the moment, but it may be due to the use of an inappropriate form of the drag force.

In figure 14, we show the particle volume fraction at the bed as a function of S^*, for $0.02 < S^* < 0.1$, calculated from the simulation. The values predicted by the simulation are in quantitative agreement with the experimental data. Comparison of the height-integrated mass flux Q is displayed in figure 15. The agreement with the experimental data is fairly good.

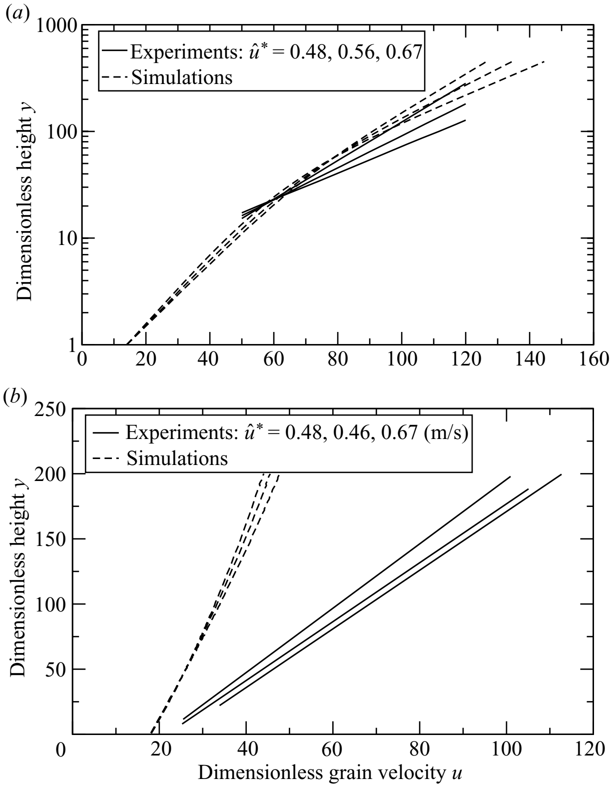

FIGURE 13. (*a*) Air velocity profiles for various friction speeds: experiments (continuous lines) and simulations (dashed lines). (*b*) Corresponding particle velocity profiles: experiments (continuous lines) and simulations (dashed lines). The parameters used in the simulation are $u_{0\uparrow} = 15$, $T = 40$ and $\mu = 0.8$.

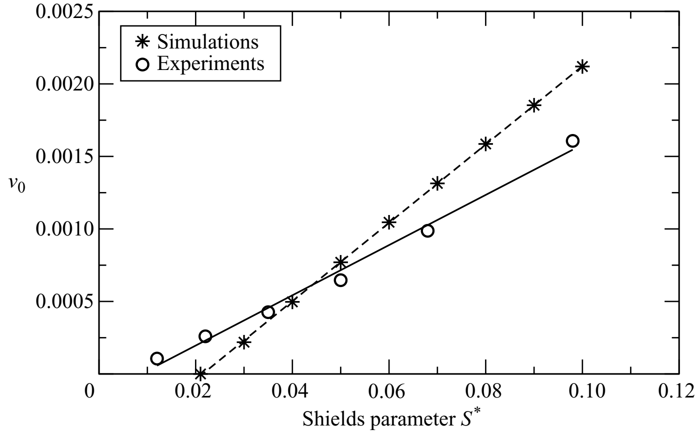

FIGURE 14. Particle volume fraction at the bed as a function of the Shields parameters: comparison between experimental data and simulations. The parameters used in the simulation are $u_{0\uparrow} = 15$, $T = 40$ and $\mu = 0.8$.

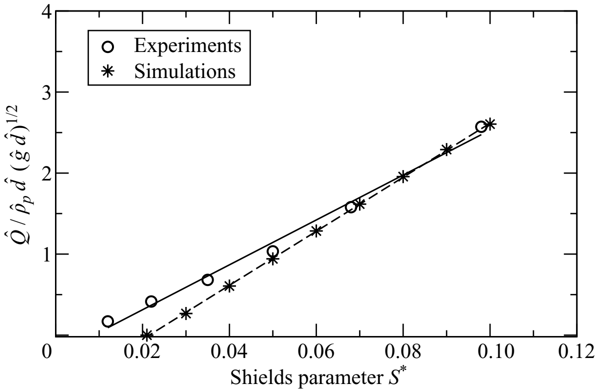

FIGURE 15. Dimensionless mass flow rate $\hat{Q}/(\hat{\rho}_p\hat{d}\sqrt{\hat{g}\hat{d}})$ as a function of the Shields parameter: comparison between experiment data and simulations. The parameters used in the simulation are $u_{0\uparrow}=15$, $T=50$ and $\mu=0.8$.

5. Conclusion

The results of combined measurements of the distributions of concentration, particle velocity and air velocity above a particle bed have been reproduced using a numerical simulation that employs half-Gaussian velocity distributions for the upward and downward particles, with the unknown parameters of the distributions determined using low moments of the splash function measured in experiments. The success of this simple representation eliminates the need to consider the complete splash function or more general velocity distribution functions and places the description of saltation closer to that employed for collisional flows.

The experiments reported provide a complete set of measurements characterizing saltating particles, including particle concentration, particle velocity and mass flux profiles. The correctness of those particle velocity measurements was ensured by the use of three different methods of measurement. The comparison between the results of the three methods highlighted the limitations of PIV in this context. However, despite the sophistication of the measurement techniques, the measurement of particle concentration near the bed still poses a challenge.

The calculation of the average fluxes of mass and momentum in the particle phase at the bed made use of existing measurements of the relationship between the velocity of an impinging sphere and the average of its rebound velocities and the average number of ejected spheres that were produced (see (4.11)–(4.13)). The coefficients in these dimensionless relationships are expected to depend on the restitution, friction and angularity of the particles but not on their size.

The velocity distribution of the impinging particles at the bed used to calculate the average fluxes is the simplest possible that involves three unknown parameters, which, in a steady state, can be determined by the balance of mass and the two components of momentum at the bed. Certainly, a more complicated velocity distribution is likely in reality, but it is not clear that the introduction of complications will improve the predictions.

The determination of numerical values of two of the parameters of the velocity distribution in a steady state permitted the introduction of a simple numerical simulation for the determination of the numerical value of the third. As in other more complicated numerical simulations and analytical treatments of saltation, the simulation incorporated a simple model of turbulence in the gas near the bed based on the local shear stress in the gas and the distance from the bed and neglected suspension of the particles due to the velocity fluctuations of the gas. The simulation was able to reproduce all of the qualitative features and most of the quantitative features of the particle concentration.

A quantitative difference is in the magnitude of the grain velocities. This could be related to the expression for the drag employed, the neglect of turbulent and collisional suspension or there being a distribution of particle diameters. These possible sources of the differences between the measured and predicted values of the particle velocities are presently being considered. It is hoped the results of these investigations would be reported in the near future.

The experiments were carried out by Dupont, Valance, Ould El Moctar and Rasmussen in a wind tunnel constructed by Rasmussen; the data were reduced by Creyssels, Dupont, Valance and Ould El Moctar; the boundary conditions were derived by Cantat, Jenkins and Pasini; and the numerical simulation was developed by Valance, as a simplification of a more elaborate scheme by Pasini. The research was supported by NASA Grant NAG3-2353 to Cornell University and ANR Grant ANR-05-BLAN-0273 to the University of Rennes 1 and Nantes University. Isabelle Cantat acknowledges support from the DGA (Grant ERE-05C0060).

Appendix A. Distribution of vertical velocities

Equation (4.5) projected in the y-direction gives $\mathrm{d}\xi_y/\mathrm{d}t = -1$. Write $f_{\xi_y} = \int \mathrm{d}\xi_x f(y, \xi_x, \xi_y, t)$ and derive the Boltzmann equation for this distribution with the assumption that there are no collisions between particles:

$$\frac{\partial f_{\xi_y}}{\partial t} + \xi_y \frac{\partial f_{\xi_y}}{\partial y} - \frac{\partial f_{\xi_y}}{\partial \xi_y} = 0. \tag{A1}$$

In a fully developed, steady state, the time derivative of f_{ξ_y} is zero and $\partial f_{\xi_y}/\partial \xi_y = \xi_y \partial f_{\xi_y}/\partial y$. With the boundary condition $f_{\xi_y}(0, \xi_y) = n_0 \mathrm{e}^{-\xi_y^2}/(2T_y)/\sqrt{2\pi T_y}$,

$$f_{\xi_y}(y, \xi_y) = n_0 \mathrm{e}^{-y/T_y}\, \mathrm{e}^{-\xi_y^2}/(2T_y)/\sqrt{2\pi T_y}. \tag{A2}$$

Appendix B. Flux of ejected particles

In this appendix, an approximate value is determined for

$$\Phi_{ej} = \int_{\xi_y < 0, \xi > \xi_0} f(\xi_x, \xi_y) N_{ej}(\xi_x, \xi_y) |\xi_y| \mathrm{d}\xi_y \mathrm{d}\xi_x. \tag{B1}$$

Define $\boldsymbol{\varepsilon} = \boldsymbol{\xi} - \boldsymbol{u}_0 = (\varepsilon \cos\phi, -\varepsilon \sin\phi)$ and integrate using the variables (ε, ϕ) (see figure 16). The integration domain is approximated using the assumption that particles leading to ejection impact mainly at small angle ϕ. Thus, terms of the order ϕ^2 or higher are disregarded. This approximation is valid if $\xi_0 > u_0$, as shown in figure 16.

Thus, the condition $\xi^2 > \xi_0^2$ becomes, for a given ε, $\phi < \phi_m(\varepsilon)$, with $\phi_m(\varepsilon)^2 = (u_0^2 + \varepsilon^2 - \xi_0^2 + 2u_0\varepsilon)/(u_0\varepsilon)$. Set $\delta\varepsilon = \varepsilon - \varepsilon_0$, of the order of ϕ_m^2, with $\varepsilon_0 = \xi_0 - u_0$. The domain definition allows only positive values of $\delta\varepsilon$ and, at order one in $\delta\varepsilon$, $\phi_m^2 = 2\xi_0\delta\varepsilon/[u_0(\xi_0 - u_0)]$.

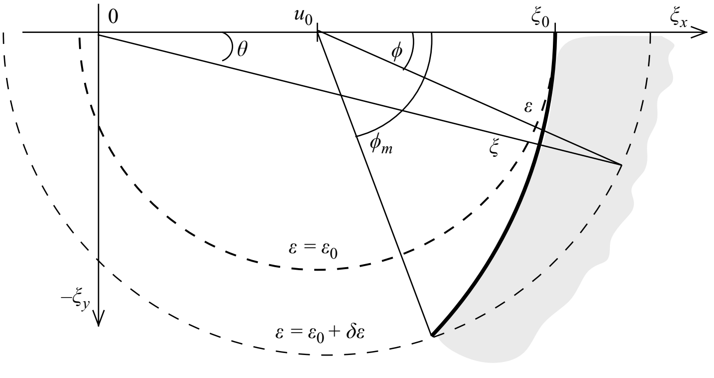

FIGURE 16. Only particles with a velocity in the grey domain (unlimited to the right) lead to bead ejection. Because the bead density decreases exponentially as ε increases, the main contribution to the integral comes from points around $\boldsymbol{\xi} = \boldsymbol{\xi_0}$, for which $\phi \ll 1$ and $\delta\varepsilon \ll \varepsilon_0$. Here, ϕ_m is the boundary of the domain and scales as $\phi_m \sim \delta\varepsilon^{1/2}$.

Express the number of ejected particles, given by (4.13), as a function of ϕ and $\delta\varepsilon$, and obtain, at order 5/2 in $\delta\varepsilon$,

$$N_0(1-A^2)(1+K\phi)\left(\frac{\delta\varepsilon}{\xi_0} - \frac{u_0\phi^2(\xi_0-u_0)}{2\xi_0^2}\right), \tag{B2}$$

with $K = 2AB(\xi_0 - u_0)/[\xi_0(1-A^2)]$. Finally,

$$\begin{aligned}\frac{2\pi T}{n}\Phi_{ej} &= N_0(1-A^2)\int_{\varepsilon=\xi_0-u_0}^{\infty}\int_{\phi=0}^{\phi_m} \varepsilon^2 \sin\phi\, \mathrm{e}^{-\varepsilon^2/2T}\left[\frac{\delta\varepsilon}{\xi_0} - \frac{u_0\phi^2(\xi_0-u_0)}{2\xi_0^2}\right](1+K\phi)\mathrm{d}\delta\varepsilon d\phi \\ &= N_0\frac{T^3}{u_0(\xi_0-u_0)^2}\mathrm{e}^{-(\xi_0-u_0)^2/2T}\left(1 - A^2 + AB\sqrt{\frac{2\pi T}{\xi_0 u_0}}\right)\end{aligned}$$

The integrations have been performed numerically for $u_0 = 20$ and $T = 20$, leading to a value 20 % smaller.

Appendix C. Flux of lost beads

The beads rebounding with a velocity $\xi_r' < \sqrt{gd} = \xi_c$ are lost. From (4.11), $\xi_r' = A\xi - B\xi\sin\theta$, and the lost beads thus satisfy $\sin\theta > A/B - \xi_c/(B\xi)$. This condition leads to $\theta \in [\theta_m, \pi - \theta_m]$, with $\theta_m = \pi$ if $\xi < \xi_1 = \xi_c/A$, $\theta_m = \arcsin[A/B - \xi_c/(B\xi)]$ if $\xi_1 < \xi < \xi_2 = \xi_c/(A-B)$ and $\theta_m = \pi/2$ if $\xi_1 < \xi_2$. The resulting integration domain is shown in figure 17.

The density is assumed constant and equal to $\mathrm{e}^{-u_0^2/(2T)}$ for the impacting particles that will be lost after rebound. The integration is performed on ξ and θ (the impacting velocity and the impacting angle) and leads to

$$\begin{aligned}\Phi_l &= \frac{n}{2\pi T}\mathrm{e}^{-u_0^2/(2T)}\left(\int_{\xi=0}^{\xi_1}\int_{\theta=0}^{\pi}\xi^2\sin\theta\mathrm{d}\xi\mathrm{d}\theta + \int_{\xi=\xi_1}^{\xi_2}\int_{\theta=\theta_m}^{\pi-\theta_m}\xi^2\sin\theta\mathrm{d}\xi\mathrm{d}\theta\right) \\ &= 74\,\frac{n}{2\pi T}\,\xi_c^3\mathrm{e}^{-u_0^2/(2T)} \end{aligned} \tag{C1}$$

The numerical value obtained for $u_0 = 20$ and $T = 20$ is 10 % smaller.

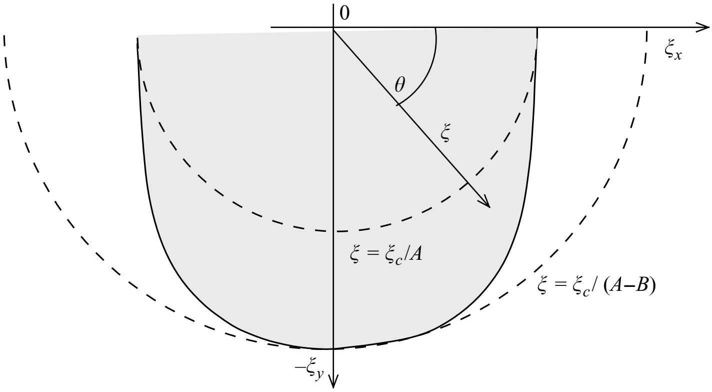

FIGURE 17. The beads with velocities in the grey domain are lost after rebound. The equation of the domain boundary is $\sin\theta > \sin\theta_m(\xi)$.

Appendix D. Shear stress

If the beads that impact the bed with a negative horizontal velocity are neglected, then

$$\begin{aligned} \xi'_{x,r} &= \xi\sqrt{e^2 - e_y^2\sin^2\theta} \\ &= \xi\left(\left(A^2 - A_y^2\right) + 2(A_yB_y - AB)\sin\theta + \left(B^2 - B_y^2\right)\sin^2\theta\right)^{0.5} \\ &\approx \sqrt{B^2 - B_y^2}\left(\frac{AB - A_yB_y}{B^2 - B_y^2}\xi - \xi_y\right). \end{aligned} \tag{D1}$$

Using the fact that $\xi = (u_0^2 + \varepsilon^2 + 2u_0\varepsilon\cos\phi)^{0.5}$, the integral expression for the stress is

$$\begin{aligned} s_0 = \frac{mn_0}{2\pi T}\int_\varepsilon\int_\phi \varepsilon^2\sin\phi\, \mathrm{e}^{-\varepsilon^2/2T}\Bigg(& u + \varepsilon\cos\phi + \sqrt{B^2 - B_y^2}\varepsilon\sin\phi \\ & -\frac{AB - A_yB_y}{\sqrt{B^2 - B_y^2}}(u^2 + \varepsilon^2 + 2u\varepsilon\cos\phi)^{0.5}\Bigg)\mathrm{d}\varepsilon\mathrm{d}\phi, \end{aligned} \tag{D2}$$

which yields

$$s_0 \approx \nu_0 T\left(0.5\sqrt{B^2 - B_y^2} + \left(1 - \frac{AB - A_yB_y}{\sqrt{B^2 - B_y^2}}\right)\frac{1}{\sqrt{2\pi}}\frac{u}{\sqrt{T}} + \frac{AB - A_yB_y}{\sqrt{B^2 - B_y^2}}\frac{1}{\sqrt{2\pi}}\frac{\sqrt{T}}{u}\right) \tag{D3}$$

in the limit where

$$\frac{A^2 - A_y^2}{B^2 - B_y^2} - \frac{(AB - A_yB_y)^2}{\left(B^2 - B_y^2\right)^2} \ll 1.$$

Equation (D3) furnishes an approximate estimation. The error made is less than 5 % when compared with the exact numerical integration. Using the parameters of the splash function obtained by Beladjine *et al.* (2007) together with the fact $u_0/\sqrt{T} = \sqrt{\pi/2}(1 + B_y)/A_y$, we obtain $s = 0.6\,\nu_0 T$.

REFERENCES

ANDERSON, R. S. & HAFF, P. K. 1988 Simulation of aeolian saltation. *Science* **241**, 820–823.

ANDERSON, R. S. & HAFF, P. K. 1991 Wind modification and bed response during saltation of sand in air. *Acta Mech.* **1** (Suppl.), 21–52.

ANDERSON, R. S., SØRENSEN, M. & WILLETTS, B. B. 1991 A review of recent progress in our understanding of aeolian transport. *Acta Mech.* **1** (Suppl.), 1–20.

ANDREOTTI, B. 2004 A two-species model of aeolian sand transport. *J. Fluid Mech.* **510**, 47–70.

BAGNOLD, R. A. 1941 *The Physics of Blown Sand and Desert Dunes*. Chapman and Hall/Methuen.

BELADJINE, D., AMMI, M., OGER, L., VALANCE, A. & BIDEAU, D. 2007 An experimental study of the collision process of a grain on a two-dimensional granular bed. *Phys. Rev.* E **75**, 61305–61317.

CERCIGNANI, C. 1988 *The Boltzmann Equation and Its Applications*. Springer.

DURAN, O. & HERRMANN, H. 2006 Modeling of saturated sand flux. *J. Stat. Mech.*, **7**, P07011.

HUNT, J. R. C., EAMES, I. & WESTERWEEL, J. 2006 Mechanics of inhomogeneous turbulence and interfacial layers. *J. Fluid Mech.* **554**, 499–519.

IVERSEN, J. D. & RASMUSSEN, K. R. 1999 The effect of wind speed and bed slope on sand transport. *Sedimentology* **46**, 723–731.

JENKINS, J. T. & HANES, D. M. 1998 Collisional sheet flows of sediment driven by a turbulent fluid. *J. Fluid Mech.* **370**, 29–52.

KIND, R. J. 1976 A critical examination of the requirements for model simulation of wind-induced erosion/deposition phenomena such as snow drifting. *Atmos. Environ.* **10**, 219–227.

LIU, X. & DONG, Z. 2004 Vertical profiles of aeolian sand mass flux. *Geomorphology* **59**, 205–219.

MCKENNA-NEUMAN, C. & MALJAARS, M. 1997 Wind tunnel measurement of boundary layer response to sediment transport. *Bound. Layer Meteorol.* **84**, 67–83.

MITHA, S., TRAN, M. Q., WERNER, B. T. & HAFF, P. K. 1986 The grain/bed impact process in aeolian saltation. *Acta Mech.* **63**, 267.

NAMIKAS, S. L. 2003 Field measurement and numerical modeling of aeolian mass flux distributions on a sandy beach. *Sedimentology* **50**, 303–326.

NAPALNIS, P., HUNT, J. C. R. & BARRETT, C. F. 1993 Saltating particles over flat beds. *J. Fluid Mech.* **251**, 661–685.

NISHIMURA, K. & HUNT, J. C. R. 2000 Saltation and incipient suspension above a flat particle bed below a turbulent boundary layer. *J. Fluid Mech.* **417**, 77–102.

OGER, L., AMMI, M., VALANCE, A. & BELADJINE, B. 2005 Discrete element method studies of the collision of one rapid sphere on 2D and 3D packings. *Eur. Phys. J.* E **17**, 467–476.

OWEN, P. R. 1964 Saltation of uniform grains in air. *J. Fluid Mech.* **20**, 225–242.

OWEN, P. R. 1980 *The Physics of Sand Movement*. Lecture notes. Workshop on Physics Desertification. International Centre for Theoretical Physics, Trieste.

PASINI, J. M. & JENKINS, J. T. 2005 Aeolian transport with collisional suspension. *Phil. Trans. R. Soc. Lond.* **363**, 1625–1646.

PTASINSKI, P. K., BOERSMA, B. J., NIEUWSTADT, F. T. M., HULSEN, M. A., VAN DEN BRULE, B. H. A. A. & HUNT, J. C. R. 2003 Turbulent channel flow near maximum drag reduction: simulations experiments and mechanisms. *J. Fluid Mech.* **490**, 251–291.

RASMUSSEN, K. R. & MIKKELSEN, H. E. 1991 Wind tunnel observations of aeolian transport rates. *Acta Mech.* **1** (Suppl.), 135–144.

RASMUSSEN, K. R. & MIKKELSEN, H. E. 1998 On the efficiency of vertical array aeolian field traps. *Sedimentology* **45**, 789–800.

RASMUSSEN, K. R. & SØRENSEN, M. 2005 *Dynamics of Particles in Aeolian Saltation: Powder and Grains* (Ed. R. Garcia-Rojo, H. J. Herrmann & S. McNamara) pp. 967–971. A. A. Balkema Publishers.

RICE, M. A., WILLETTS, B. B. & MCEWAN, I. K. 1996 Observations of collisions of saltating grains with a granular bed from high-speed cine-film. *Sedimentology* **43**, 21–31.

RICHMAN, M. W. 1988 Boundary conditions based on a modified Maxwellian velocity distribution for flows of identical, smooth, nearly elastic spheres. *Acta Mech.* **75**, 227–240.

RIOUAL, F., VALANCE, A. & BIDEAU, D. 2000 Experimental study of the collision process of a grain on a two-dimensional granular bed. *Phys. Rev.* E **62**, 2450.

SAUERMANN, G., KROY, K. & HERRMANN, H. J. 2001 Continuum saltation model for sand dunes. *Phys. Rev.* E **64**, 031305.

Sørensen, M. 1991 An analytic model of wind blown sand transport. *Acta Mech.* **1** (Suppl.), 67–81.

Sørensen, M. 2004 On the rate of aeolian sand transport. *Geomorphology* **59**, 53–62.

Sørensen, M. & McEwan, I. 1996 On the effect of mid-air collisions on aeolian saltation. *Sedimentology* **43**, 65–76.

Ungar, J. & Haff, P. K. 1987 Steady state saltation in air. *Sedimentology* **34**, 289.

Werner, B. T. 1990 A steady-state model of wind-blown sand transport. *J. Geol.* **98**, 1–17.

Werner, B. T. & Haff, P. K. 1988 The impact process in aeolian saltation: two-dimensional simulations. *Sedimentology* **35**, 189.

White, B. R. & Mounla, H. 1991 An experimental study of froude number effect on wind-tunnel saltation. *Acta Mech.* **1** (Suppl.), 145–157.

White, B. R. & Schulz, J. C. 1977 Magnus effect in saltation. *J. Fluid Mech.* **81**, 497–512.

Willetts, B. B. & Rice, M. A. 1989 Collision of quartz grains with a sand bed: the influence of incident angle. *Earth Surf. Proc. Land Forms* **14**, 719–730.

Yang, P., Dong, Z., Qian, G., Luo, W. & Wang, H. 2007 Height profile of the mean velocity of an aeolian saltating cloud: wind tunnel measurements by particle image velocimetry. *Geomorphology* **89**, 320–334.